

RSC Advances



This is an *Accepted Manuscript*, which has been through the Royal Society of Chemistry peer review process and has been accepted for publication.

Accepted Manuscripts are published online shortly after acceptance, before technical editing, formatting and proof reading. Using this free service, authors can make their results available to the community, in citable form, before we publish the edited article. This *Accepted Manuscript* will be replaced by the edited, formatted and paginated article as soon as this is available.

You can find more information about *Accepted Manuscripts* in the [Information for Authors](#).

Please note that technical editing may introduce minor changes to the text and/or graphics, which may alter content. The journal's standard [Terms & Conditions](#) and the [Ethical guidelines](#) still apply. In no event shall the Royal Society of Chemistry be held responsible for any errors or omissions in this *Accepted Manuscript* or any consequences arising from the use of any information it contains.

ARTICLE

Characterization of a P2-type chelating-agent-assisted $\text{Na}_{2/3}\text{Fe}_{1/2}\text{Mn}_{1/2}\text{O}_2$ cathode material for sodium-ion batteries

Cite this: DOI: 10.1039/x0xx00000x

Received 00th January 2012,
Accepted 00th January 2012

DOI: 10.1039/x0xx00000x

www.rsc.org/Kwangjin Park^a, Dongwook Han^a, Hyunjin Kim^{*a}, Won-seok Chang^a, Byungjin Choi^a, Benayad Anass^a and Seoksoo Lee^{*a},

A chelating-agent-assisted $\text{Na}_{2/3}\text{Fe}_{1/2}\text{Mn}_{1/2}\text{O}_2$ is studied as a cathode for sodium-ion batteries. Addition of NH_4OH results in the formation of a homogeneous powder with lower resistance and larger carbon content on the cathode surface. Formation of a thin and stable solid-electrolyte interface layer leads to its enhanced electrochemical performance.

Introduction

Recently, the global demand for lithium (Li)-ion batteries has grown quite rapidly owing to its high energy density, which makes it an attractive energy source for use in applications ranging from mobile products to high-energy-capacity devices such as electric vehicles (EV) and energy-storage systems (ESS) [1-3]. However, because of the limited amount of Li reserves on Earth (0.006 wt% abundance on Earth), its cost-effectiveness is not very high. Thus, alternative battery materials are actively sought, with extensive research interest centered on addressing this issue. The sodium (Na)-ion battery is a promising candidate owing to its low cost and high abundance on Earth compared to Li [3-4]. Over the past decades, many researchers have tried to develop a suitable material on which the fabrication of Na-ion batteries could be based. Layered transition-metal oxides such as Na_xMO_2 ($M = \text{Co}, \text{Ni}, \text{Cr}, \text{Fe}, \text{Mn}$) have attracted attention as promising candidates for cathode-active materials [1-5]. Na-based layered cathode materials can be categorized into two major groups, denoted as P2 and O3 types. The first letter "P" or "O" refers to the nature of the site occupied by the alkali ion (prismatic or octahedral), while the numeral "2" or "3" refers to the number of alkali layers in the repeat unit perpendicular to the layering [1,3-5].

Among known Na_xMO_2 materials, a P2-type $\text{Na}_{2/3}\text{Fe}_{1/2}\text{Mn}_{1/2}\text{O}_2$ (NFMO) has recently emerged as a superior material with the best capacity (190 mAh g^{-1}) between 4.2–1.5 V in 1 M NaClO_4 electrolyte [1]. However, this fascinating layered oxide cathode must still overcome several major drawbacks for its successful commercialization. The first issue to be addressed is its high initial irreversible capacity, which is thought to arise from side reactions occurring with the electrolyte [8]. The second issue is its low rate capability, possibly originating from the formation of a thick solid-electrolyte interfacial (SEI) layer on the cathode surface during cycling or from its low electronic conductivity. This phenomenon may be significantly related to the preparation method. Therefore, effecting precise control over preparation conditions or synthetic modifications is a promising strategy to overcome these drawbacks [8-9]. Many research

groups have reported that the addition of a chelating agent during synthesis enhances the electrochemical performance by increasing the uniformity of powder size and crystallinity [8-11].

In this study, the NFMO material was synthesized by a co-precipitation method using NH_4OH as the chelating agent. A 15% increase in initial capacity as well as capacity retention of 94% after 30 cycles were obtained utilizing this chelating-agent-assisted $\text{Na}_{2/3}\text{Fe}_{1/2}\text{Mn}_{1/2}\text{O}_2$ (C-NFMO). Furthermore, we also investigated the effects of the chelating agent on NFMO structure, morphology, and electrochemical performance.

Experiment

NFMO was synthesized by a co-precipitation procedure using NH_4OH as a chelating agent. $\text{Mn}(\text{SO}_4)\cdot\text{H}_2\text{O}$ and $\text{Fe}(\text{SO}_4)\cdot 7\text{H}_2\text{O}$ were dissolved in de-ionized water at 80 °C and stirred for 12 h to obtain a homogeneous solution. Next, the chelating agent (0.5 molar ratio to the metal ions) and a stoichiometric amount of NaOH solution were added. Co-precipitation occurred after sufficient stirring. The co-precipitated $(\text{Mn}_{1/2}\text{Fe}_{1/2})(\text{OH})_2$ was washed and filtered with de-ionized water. Filtered $(\text{Mn}_{1/2}\text{Fe}_{1/2})(\text{OH})_2$ was dried in an oven at 120 °C. The dried $(\text{Mn}_{1/2}\text{Fe}_{1/2})(\text{OH})_2$ powder was co-ground with a stoichiometric amount of Na_2CO_3 . Calcination of the ground material was performed at 850 °C over 12 h in air.

Determination of sample structural characteristics was performed by X-ray diffractometry (XRD) using $\text{Cu-K}\alpha$ radiation and a scan speed of $0.02^\circ \text{ min}^{-1}$ between $2\theta = 10\text{--}65^\circ$ at an applied potential of 40 kV and current of 40 mA. X-ray photoelectron spectroscopic (XPS) analyses were performed with a Physical Electronics (PHI) (Quantum 2000 Scanning ESCA Microprobe) spectrometer using a focused monochromatized $\text{Al-K}\alpha$ radiation source (1486.6 eV). To avoid any external contamination, all samples were transferred under an Ar environment from the glove box to the spectrometer using a transfer chamber. Morphological changes on the NFMO surface were investigated using a scanning electron microscope (SEM, Hitachi S-4700N).

Composite positive electrodes comprising 60 wt% active

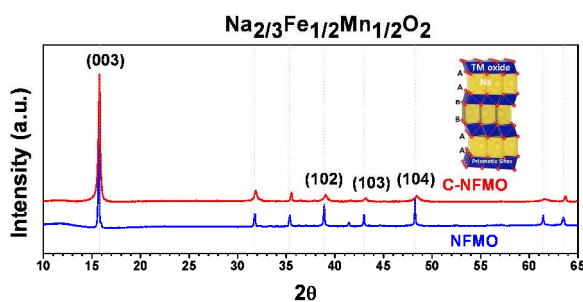


Fig.1 XRD patterns of $\text{Na}_{2/3}\text{Fe}_{1/2}\text{Mn}_{1/2}\text{O}_2$ powders prepared by co-precipitation

materials, 20 wt% DENKA BLACK[®], and 20 wt% polyvinylidene difluoride (PVDF) were pasted onto Al foil as a current collector. The electrodes were dried at 120 °C under vacuum and pressed. Metallic Na was used as the anode electrode. The electrolyte solution used was 1.0 M NaPF_6 dissolved in propylene carbonate (PC). A glass fiber was used as a separator. R2032-type coin cells were assembled in an Ar-filled glove box. Cyclic voltammetry (Model VMP3, NanoQuébec) was performed at a $10 \mu\text{Vs}^{-1}$ scan rate. For galvanostatic experiments, the cells were discharged/charged galvanostatically at a constant current.

Cathode electrochemical activities were characterized by electrochemical impedance spectroscopy (EIS) using a Solartron 1260 frequency-response analyzer with an applied frequency from 10 mHz to 1 MHz. EIS measurements were performed on the charged and discharged states during the cycle. Impedance spectra were analyzed with an equivalent circuit using the ZView[®] (Windows) software.

Results and Discussion

Figure 1 shows the XRD patterns of synthesized NFMO and C-NFMO. The two synthesized powders showed well-defined characteristics matching that of a P2-type layered structure, compared to the previous study [1]. The P2-type structure exhibited different layers of AB-BA oxygen packing, with transition metal (*Tm*) ions in octahedral sites as depicted in Figure 1. No extra reflection peaks were observed, regardless of chelating agent addition. The narrower peak full-width half-maximum indicated an improvement in the crystalline nature of the sample.

During synthesis, precipitation occurs when the aqueous acid and alkali solutions are mixed together. Upon the addition of a chelating agent, homogeneous $[\text{Mn}_{1/2}\text{Fe}_{1/2}(\text{NH}_3)_n]^{2+}$ is formed with a stoichiometric ratio of Mn and Fe (Eq. (1)), which facilitates the formation of a homogeneous $\text{MnFe}(\text{OH})_2$ phase in the precipitation process (Eq. (2)):

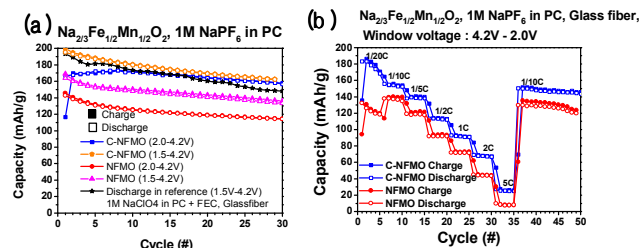
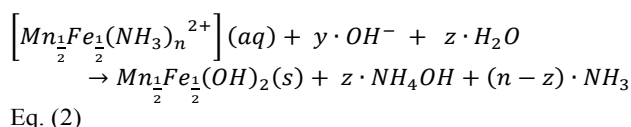
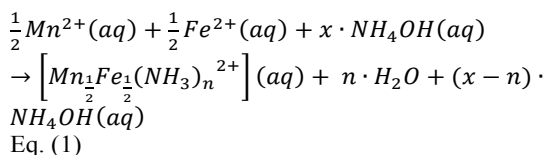


Fig.2 (a) Cycling performance comparison of NFMO and C-NFMO. (b) Comparison of rate capabilities of NFMO and C-NFMO

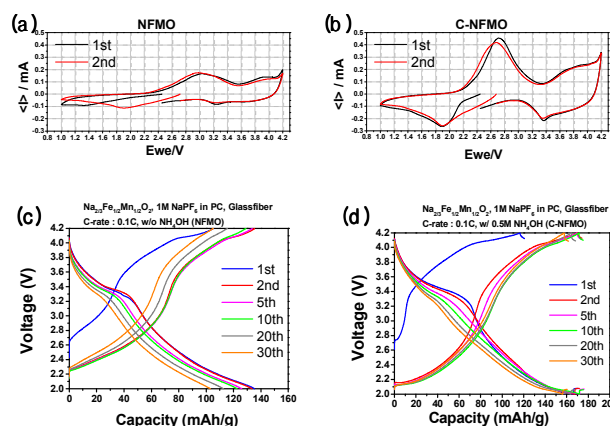


Fig.3 Cyclic voltammograms: (a) NFMO, (b) C-NFMO. Typical charge–discharge characteristics: (c) NFMO, (d) C-NFMO.

Therefore, the formation of by-products as a result of phase separation – $\text{Mn}(\text{OH})_2$ and $\text{Fe}(\text{OH})_2$ – are prevented, and a well-defined metal hydroxide is acquired using a chelating agent, resulting in the synthesis of a homogeneous, highly crystalline NFMO powder.

Figure 2(a) compares the cycling performance of the cells cycled at 25 °C with a constant rate of 0.1C. At a cutoff voltage of 1.5 V, the cells delivered reversible capacities of $\sim 165 \text{mAh}\cdot\text{g}^{-1}$ and $\sim 195 \text{mAh}\cdot\text{g}^{-1}$ for NFMO and C-NFMO, respectively. When the cutoff voltage was increased to 2.0 V, NFMO and C-NFMO displayed capacities of $\sim 145 \text{mAh}\cdot\text{g}^{-1}$ and $\sim 166 \text{mAh}\cdot\text{g}^{-1}$, respectively. The initial capacity of C-NFMO corresponded to an increase of about 14% compared to NFMO, regardless of cutoff voltage. The capacity retention of C-NFMO was found to be similar to that of NFMO under the 1.5 V voltage cutoff conditions. This result might be due to the phase transition as the result of a stacking fault, in which the octahedral and prismatic layers are piled up along the *c*-axis direction, which effectively decreases repulsion between Na ions [1,12]. On the other hand, the capacity fading of C-NFMO was much slower than that of NFMO, with a capacity retention of 94% at 0.1C at 30 cycles at a cutoff voltage of 2.0 V; this corresponds to an improvement in capacity retention of greater than 20%, compared to that for NFMO. The cyclic performance is clearly improved with the incorporation of a chelating agent during preparation.

NFMO rate capabilities were next evaluated by cycling at various rates from 0.05–5C, and the results are presented in Figure 2(b). As the applied current was increased, the capacities of all samples decreased; this observation can be ascribed to an increase in over-potential resulting from the lack of reaction

time for mobile cation intercalation into the crystal lattice, as only the surface of the active materials participates in the reaction [7]. After C-rate tests, the original capacities of both samples were restored.

The electrochemical reactions of NFMO and C-NFMO were confirmed by cyclic voltammetry analyses, and the resulting cyclic voltammograms are shown in Figures 3(a) and (b), respectively. For NFMO, two anodic peaks at 2.78 V and 3.95 V, and two cathodic peaks at 1.88 V and 3.25 V were observed, which corresponds to the intercalation and extraction processes of mobile Na^+ ions, respectively. On the other hand, for C-NFMO, the anodic peaks were shifted to a lower voltage (2.68 V and 3.88 V), while the cathodic peaks experienced a similar shift to higher voltage (1.89 V and 3.37 V), indicative of the improved kinetic properties. The lower cathodic peak is related to the $\text{Mn}^{3+}/\text{Mn}^{4+}$ redox process, while the higher cathodic peak is concerned with the $\text{Fe}^{3+}/\text{Fe}^{4+}$ redox. The sharp increase in the anodic curve at around 4.2 V is related to a quasi-reversible P2-type-to-O2-type phase transition occurring at low Na content in the material [1,5,7].

Figures 3(c) and (d) show the potential versus capacity profiles of NFMO and C-NFMO during the 1st, 2nd, 5th, 10th, 20th and 30th cycles at 0.1C, with profiles for both materials showing a similar slope as well as other features. The location of the potential plateau was consistent with the results of cyclic voltammetry experiments; the profile for C-NFMO exhibited a wider plateau than bare NFMO, indicating the existence of more reaction sites. The capacity fading for the two samples can be mostly attributed to the decrease in the high potential plateaus, especially those at around 3.4 V. However, the capacity fading of C-NFMO at 30 cycles is much smaller than that of NFMO.

During the intercalation process, Na^+ ions can be inserted into two different types of trigonal prismatic sites: Na_f and Na_e , where Na_f shares faces with two TmO_6 octahedra of adjacent slabs, while Na_e shares edges with six surrounding TmO_6 octahedra. This phenomenon of partial interchange in the occupancy of Na^+ and transition-metal ions among the sites is referred to as “cation mixing” [7,11]. When cation mixing occurs, the capacity fading gradually increases due to lower diffusivity of the mobile ion in conjunction with an increase in electronic resistance [12]. Unfortunately, Mn and Fe materials possess higher probabilities of cation mixing in the layered structure compared to other transition metals such as Co, Ni, V and Cr [12]. The probability of cation mixing can be confirmed by examining the integrated ratio of the (003) to (104) peak in the XRD pattern, where the (003) peak appears as the result of diffraction of the layered rock-salt structure (R-3m), whereas the (104) peak appears as the result of diffractions of layered and cubic rock-salt structures [13]. A value of $I_{(003)}/I_{(104)} < 1.2$ is indicative of a high probability of cation mixing [11-14].

The $I_{(003)}/I_{(104)}$ peak ratios of NFMO and C-NFMO were calculated to be 1.3 and 4.8, respectively, indicating a low probability of cation mixing for both materials. In particular, the value for C-NFMO was much larger than that of bare NFMO, suggesting that the chance for cation mixing in C-NFMO is much smaller than that of NFMO. Thus, this high crystallinity attributed to C-NFMO may contribute to the increased capacity and improved cycle performance by reducing the probability of cation mixing and formation of impurity phases.

SEM images of NFMO and C-NFMO are shown in Figures 3(a) and (b), respectively, in which a very distinct difference in particle size distribution could be observed between the two

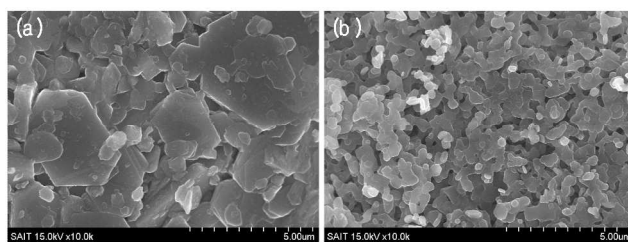


Fig.4 SEM images of $\text{Na}_{2/3}\text{Fe}_{1/2}\text{Mn}_{1/2}\text{O}_2$ powders: (a) NFMO (b) C-NFMO.

Table.1 Elemental compositions of NFMO and C-NFMO using EDX analysis.

Element (At%)	Na	Mn	Fe	O	C
NFMO	14.85	28.55	30.08	22.33	4.18
C-NFMO	16.52	25.73	23.77	25.81	8.16

materials. NFMO appeared moderately aggregated, with particles sizes of ca. 2–4 μm in diameter; C-NFMO, in contrast, was fairly homogeneous, with particle sizes of less than 1 μm in diameter. The surface areas of NFMO and C-NFMO as measured by the Brunauer–Emmett–Teller (BET) method were 4.158 m^2g^{-1} and 6.761 m^2g^{-1} , respectively. The uniform and small particle size for C-NFMO may be ascribed to the co-precipitation procedure, which is known to result from the preparation of a homogeneous precursor solution by use of chelating agent [14-15].

EDX analyses were performed to investigate particle surface compositions, the results of which are shown in Table 1. Surface elemental compositions of the two samples were almost identical, with the exception of carbon; the carbon content on the C-NFMO surface was twice the amount found on the NFMO surface. The electrical conductivities of NFMO and C-NFMO, as measured by the four-point probe method, were $1.978 \times 10^{-6} \text{ S}\cdot\text{cm}^{-1}$ and $2.296 \times 10^{-5} \text{ S}\cdot\text{cm}^{-1}$, respectively. The electronic conductivity of NFMO with smaller powder size is $2.65 \times 10^{-6} \text{ S}/\text{cm}$, which is slight higher than NFMO, but still one order of magnitude smaller than C-NFMO. The higher conductivity of C-NFMO is attributed to a larger amount of carbon on the powder surface as well as the close packing of C-NFMO particles resulted from the small particle size.

To obtain further information on the SEI layer formed on cathode surface, XPS analyses were performed after the 1st and 30th charge–discharge cycles. All samples are prepared after discharging until 2.0 V. The Fe 2p peaks and C 1s peaks are shown in Figures 4(a) and (b), respectively. Considering that the X-ray-excited photoelectrons escaped only from the uppermost surface layer (~10 nm), a smaller number of Fe 2p photoelectrons observed after 30 cycles suggested that the NFMO electrode was sufficiently buried beneath the SEI layer. In contrast, XPS results for C-NFMO saw the appearance of Fe 2p peaks in the same position although in weaker intensities. In both samples, the Fe 2p peak region showed an overlap with the F KLL Auger transition resulting from the deposition of NaF-like species during the salt decomposition process; this may be due to the formation of a thicker SEI layer on the cathode surface of NFMO [18].

The core C 1s XPS peak (284.8 eV) was assigned to graphite in the electrode. Other components were located at higher binding energies: peaks at ~289.1 eV and ~290.2 eV were assigned to CO_3 and $-\text{CF}_2$ environments, respectively. After the first

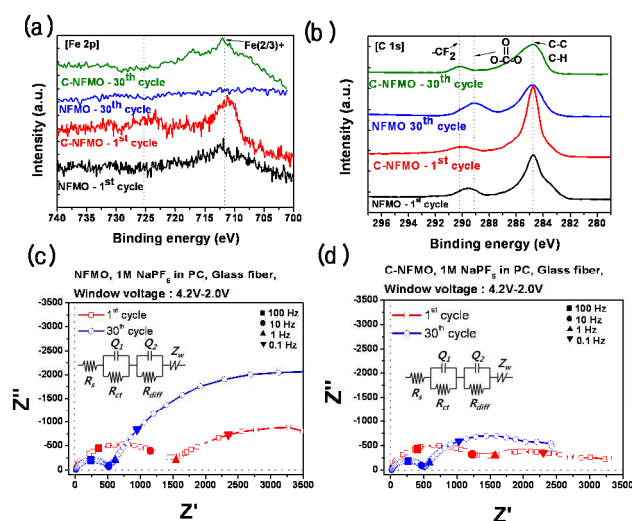


Fig.5 XPS core peaks of NFMO and C-FNMO at the 1st and 30th cycles: (a) Fe 2p and (b) C 1s. AC impedance spectra: (c) NFMO (d) C-NFMO.

charge–discharge cycle, the two samples showed almost graphite peak and $-CF_2$ peak. However, the main C 1s peak intensity at ~ 285.7 eV for NFMO increased due to the deposition of polymeric materials associated with PC decomposition to form Na_2CO_3 and aliphatic carbon or alkyl – OH species after testing over 30 cycles. The formed Na_2CO_3 acts as resistance so that capacity fading for the sample using NFMO is faster compared to that using C-NFMO.

EIS tests were next conducted to investigate differences in electrochemical polarization effects between the pristine and chelating-agent-assisted materials. The impedance of a two-electrode coin cell was measured before and after cycle tests. The circuit and EIS plots are depicted in Figures 4(c) and (d), respectively. The measured EIS can be divided into three parts composed of frequency regions similar to a Li-ion battery system, where each part is related to the charge–discharge process. The DC resistance (R_s in the equivalent circuit) mainly arises from the resistance of the electrolyte. Impedance in the intermediate-frequency region, i.e., charge transfer resistance (R_{ct}), is related to the charge transfer in the cathode–electrolyte interface. Impedance in the low-frequency region, i.e., diffusion resistance (R_{diff}), is attributed to both the migration of Na^+ ions through the SEI film and diffusion of Na^+ in the electrolyte, a phenomenon referred to as Warburg impedance [11,13–16].

The charge-transfer resistance (R_{ct}) is shown in the first semicircle in the middle-frequency regions in Figures 4 (c) and (d). The resistances of both samples were almost similar since the cathode materials have equal material composition, regardless of the assistance of a chelating agent during preparation. After the 30th charge–discharge test, radii of the first semicircles for both samples decreased, as shown in Figures 5 (c) and (d); this is attributed to the activation of NFMO during cycling, since the electrolyte diffuses into the cathode material. The lower resistance comes from the enhanced contact area between the electrolyte and cathode electrode and the stabilized layer of cathode material.

On the other hand, diffusion resistance (R_{diff}), represented by the second semicircles in the low-frequency region, showed a significant difference. After 30 cycle tests, the semicircle radius of the bare sample was much larger than that of C-NFMO. The reason for this result is that a thicker SEI layer or insulating

layer is formed on the bare NFMO when compared to C-NFMO, which hinders the Na^+ migration, in agreement with XPS results. A stable SEI layer can be achieved through surface treatment of the active material, e.g., carbon coating [17]. The higher amount of carbon on the C-MFMO surface might play a role as a carbon coating, which leads to the prevention of direct contact between the cathode material and electrolyte, as confirmed by XPS and impedance analysis.

Conclusions

The synthesis, characterization, and electrochemical performance of a P2-type $Na_{2/3}Fe_{1/2}Mn_{1/2}O_2$ material prepared via the chelating-agent effect have been described, and its potential as a cathode material for Na-ion batteries was also investigated. Addition of the chelating agent (NH_4OH) during the synthesis process allowed for the preparation of uniform and homogeneous particles with twice the amount of surface carbon as bare samples, resulting in a lower resistance and enhanced powder surface area. XPS and EIS analyses confirmed that a thinner and more stable SEI layer is formed on the surface of the chelating-assisted NFMO cathode materials after cycling tests. These effects are shown to contribute to the enhanced electrochemical performance of chelating-agent-assisted NFMO. C-NFMO showed a higher discharge capacity ($167 \text{ mAh}\cdot\text{g}^{-1}$) and an improved capacity retention of 94% at 0.1C after 30 cycles. The increased initial capacity and capacity retention of C-NFMO were calculated as ca. 15% and 20%, respectively, compared to bare NFMO.

Notes and references

^a Samsung Advanced Institute of Technology (SAIT), Samsung Electronics, Mt. 14-1, Nongseo-dong, Giheung-gu, Yongin-si, Gyeonggi-do 446-712, Republic of Korea. Fax: +82-31-8061-1319; Tel: +82-31-8061-1250; E-mail: ydmj79.park@samsung.com

* Corresponding author, E-mail: seoksoo.lee@samsung.com, hyunjin1.kim@samsung.com

- N. Yabuuchi, M. Kajiyama, J. Iwatate, H. Nishikawa, S. Hitomi, R. Okuyama, R. Usui, Y. Yamada, S. Komaba, *Nat. Mater.*, 2012, **11**, 512
- V. Palomares, P. Serras, I. Villaluenga, K. Hueso, J. Carretero-González, R. Teófilo, *Energy Environ. Sci.*, 2012, **5**, 512.
- S. Komba, C. Takei, T. Nakayama, A. Ogata, N. Yabuuchi, *Electrochem. Commun.*, 2010, **12**, 355.
- E. Hosono, T. Saito, J. Hoshino, M. Okubo, Y. Saito, D. Nishio-Hamane, T. Kudo, H. Zhou, *J. Power Sources*, 2012, **217**, 43.
- R. Berthelot, D. Carlier, C. Delmas, *Nat. Mater.*, 2011, **10**, 74.
- D. Hamani, M. Ati, J. Tarascon, P. Rozier, *Electrochem. Commun.*, 2011, **13**, 938.
- D. Lee, J. Xu, Y. Meng, *Phys. Chem. Chem. Phys.*, 2013, **15**, 3304.
- T. Zhao, S. Chen, L. Li, X. Zhang, R. Chen, I. Belharouak, F. Wu, K. Amine, *J. Power Sources*, 2013, **228**, 206.
- R. Santhanam, B. Rambabu, *J. Power Sources*, 2010, **195**, 4313.
- M. Lee, Y. Kang, S. Myung, Y. Sun, *Electrochim. Acta*, 2004, **50**, 939.
- K. Karthikeyan, S. Amaresh, G.W. Lee, V. Aravindan, H. Kim, K. Kang, W. Kim, Y. Lee, *Electrochim. Acta*, 2012, **68**, 246.
- S. Kim, X. Ma, S. Ong, G. Ceder, *Phys. Chem. Chem. Phys.*, 2012, **14**, 15571.

- 13 J. Morales, C. Pérez-Vicente, J.L. Tirado, *Mater. Res. Bull.*, 1990, **25**, 623.
- 14 Y. Makimura, T. Ohzuku, *J. Power Sources*, 2003, **119–121**, 156.
- 15 S. Kandhasamy, P. Singh, S. Thurgate, M. Ionescu, D. Appadoo, M. Minakshi, *Electrochim. Acta*, 2012, **82**, 302.
- 16 K. Karthikeyan, S. Amaresh. V. Aranvindan, W. Kim, K. Nam, X. Yang, Y. Lee, *J. Power Sources*, 2013, **232**, 240.
- 17 H. Kim, M. Kong, K. Kim, I. Kim, H. Gu, *J. Power Sources*, 2007, **171**, 917.
- 18 S. Leroy, H. Martinez, R. Dedryvère, D. Lemordant, D. Gonbeau, *Appl. Surf. Sci.*, 2007, **253**, 4895.